SPACE DEBRIS REMOVAL WITH SUB-TETHERED NET: A FEASIBILITY STUDY AND PRELIMINARY DESIGN

K. Stadnyk, K. Hovell, and L. Brewster

Obruta Space Solutions Corp., 1-589 1/2 Bank St., ON, CA, Email: {kevinstadnyk, kirkhovell, lucasbrewster}@obruta.com

ABSTRACT

With the global commercialization of space, objects are being launched into Earth's orbit faster than natural effects are deorbiting them. Orbital debris is dangerous, as the high velocities of orbiting objects typically results in fatal collision events for both parties involved, and cascading collisions between orbiting objects creates the potential for exponential debris growth. To ensure the long-term accessibility of space, high-risk objects must be actively removed to limit growth of the orbital debris population. One approach to active debris removal is with the use of a tethered-net to capture and tow an object out of orbit. This work presents the feasibility and preliminary design of a system capable of capturing an orbiting object using a tethered-net and actively deorbiting it.

Keywords: Obruta; space debris; active debris removal; deorbit; tether; net; deployment.

1. INTRODUCTION

This section describes the history and future trends of orbital debris and the problems it poses to the orbital environment. It outlines current trends and the choices behind Obruta's tethered-net approach to active debris removal.

1.1. Background

The term orbital debris refers to objects in orbit around Earth that are not considered useful. Due to the vastness of space, orbital debris was thought to pose no risk to future spacefaring missions until proven otherwise by Donald J. Kessler in 1978 [1]. Known as the Kessler Syndrome, Kessler stated that eventual collisions between orbital objects will lead to sequential collisions, producing new debris, and ultimately creating a chain reaction that will grow the debris population faster than it can naturally decay.

As of January 2021, the European Space Agency's (ESA) Space Debris Office at the European Space Operations Center (ESOC) estimates that 10,680 satellites have been launched into orbit[1]. Of these satellites, an estimated 6,250 of them are still in orbit, with only 3,700 of them are operational. Large pieces of debris commonly occurs in the form of fragmented spacecraft pieces, spent launch vehicle stages, and nonoperational satellites. ESA's Space Debris Office reports that there are approximately 28,210 of these objects tracked by global Space Surveillance Networks and maintained in their catalog, which equates to 9,200 tonnes of mass in Earth's orbit. Furthermore, many objects are too small to be tracked. These include small fragments of paint from satellites, which over time erode due to solar wind and friction from Earth's upper atmosphere. Collisions between these paint flecks, micrometeorites, and other small debris pieces are quietly increasing the total debris population.

Figure 1 offers a visual summary reported by the National Aeronautics and Space Administration (NASA) Orbital Debris Program Office of all orbital objects officially cataloged by the United States of America's Space Surveillance Network as of May 2019 [2]. Fragmentation Debris encompasses all satellite and anomalous event debris, while mission-related debris encompasses all objects intentionally separated from the spacecraft as part of a planned mission. It is important to note that only the fragmentation debris (pink), mission-related debris (orange), and rocket bodies (green) lines are considered orbital debris. Spacecraft still in orbit (blue) account for nearly one quarter of all tracked orbital objects. The amount of fragmented debris vastly outnumbers the combined total of spacecraft, rocket bodies, and mission-related debris. This is largely due to two events in particular as seen by the two large spikes in the fragmentation debris plot. The first of these events occurred on January 11$^{\text{th}}$ 2007 when the People's Republic of China conducted a successful anti-satellite missile test using one of their inoperative weather satellites [3]. The second event occurred on February 10$^{\text{th}}$ 2009 between the operational US communications satellite Iridium 33 and Cosmos 2251 satellites [4]. Due to the extremely high relative velocities of orbital objects, orbital collisions can inject hundreds to thousands of new debris pieces with each occurrence.

[1] 'Space debris by the numbers', *The European Space Agency*, 2021, https://www.esa.int/Safety_Security/Space_Debris/Space_debris_by_the_numbers (accessed 10/03/2021)

Proc. 8th European Conference on Space Debris (virtual), Darmstadt, Germany, 20–23 April 2021, published by the ESA Space Debris Office
Ed. T. Flohrer, S. Lemmens & F. Schmitz, (http://conference.sdo.esoc.esa.int, May 2021)

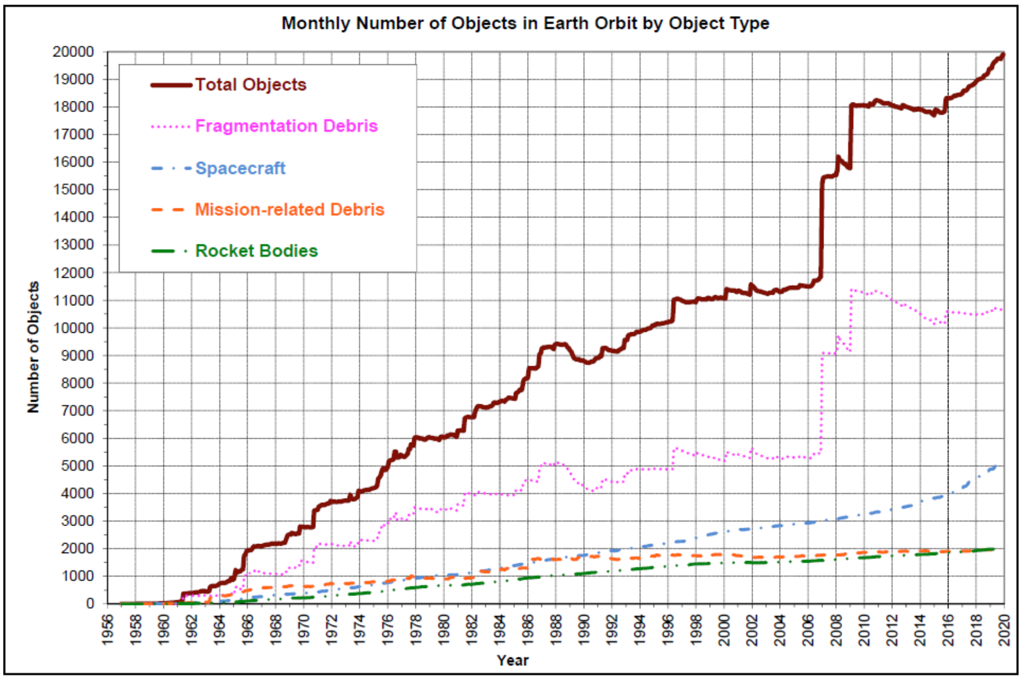

Figure 1. Monthly number of objects in Earth orbit by object type [2].

To help combat the future increase of orbital debris, the Inter-Agency Space Debris Coordination Committee (IADC) enacted guidelines recommending that all space-faring organizations ensure their orbital objects will naturally decay, or are maneuvered to an orbit in which the object will decay back to Earth, within 25 years of mission completion [5]. Currently, these are only guidelines and are not strictly enforced in the event complications arise before a satellite can be positioned to deorbit within the 25-year time frame.

Figure 2 shows a projection of the effective debris population of objects greater than 10 cm in diameter over time when adhering to no, or various, deorbiting rules with a 90% effectiveness Post Mission Disposal (PMD) rate. This projection shows that the current 25-year rule for deorbiting will result in 10% more objects remaining in orbit over the next 200 years when compared to a much lower rule of 5-years. Cost is a factor in the decision for the enacted 25-year rule, with one facet of the reasoning being that a modest, near linear increase in propellant for deorbiting is needed to reduce the residual lifetime for orbiting objects to the 50-to-25-year range, while decreasing the post-mission orbital lifetime from 25 years to 5 years or less will lead to a rapid non-linear increase in fuel requirements. Therefore, the 25-year rule still appears to be a good balance between the high costs associated with fuel and the benefit of deorbiting debris [2].

Figure 3 highlights that collision fragments are the major contributor to the overall debris population. The best approach to sustain the overall debris population is to mitigate and prevent collisions. According to a NASA model, 5-10 high-risk debris objects need to be removed from orbit each year to stabilize the low Earth orbit (LEO) environment [6]. Obruta's approach to space debris removal considers this, and is the driving factor behind our technology's capability to deorbit any orbital object regardless of if it was designed to be deorbited. Capabilities for deorbiting legacy satellites, launch vehicle bodies, and other debris that was never intended to be captured will be a key technology in achieving and maintaining a sustainable orbital environment.

1.2. Recent Developments

Developments in the field of active debris removal have begun to accelerate. The first notion of this movement within the last few years was the RemoveDEBRIS satellite research project lead by the Surrey Space Centre. RemoveDEBRIS launched in April 2018 where it demonstrated vision-based navigation, and for the first time, both space-based net deployment and capture in addition to tethered-harpoon deployment and capture[2].

SpaceLogistics, a wholly-owned subsidiary of Northrop Grumman Innovation Systems has unofficially began the commercial on-orbit servicing market—of which active debris removal is a part of—with their Mission Extension Vehicle (MEV) spacecraft. Specifically the MEV-1, this spacecraft launched on October 9$^{\text{th}}$ 2019, and successfully rendezvoused and docked with Intelsat 901 satellite on February 25$^{\text{th}}$ 2020[3]. The MEV-1 is now performing re-positioning and life-extension services for Intelsat

[2] 'RemoveDebris', *ESA Earth Observation Portal*, https://directory.eoportal.org/web/eoportal/satellite-missions/r/removedebris (accessed 25/03/2021)

[3] 'MEV-1 and MEV-2', *ESA Earth Observation Portal*,

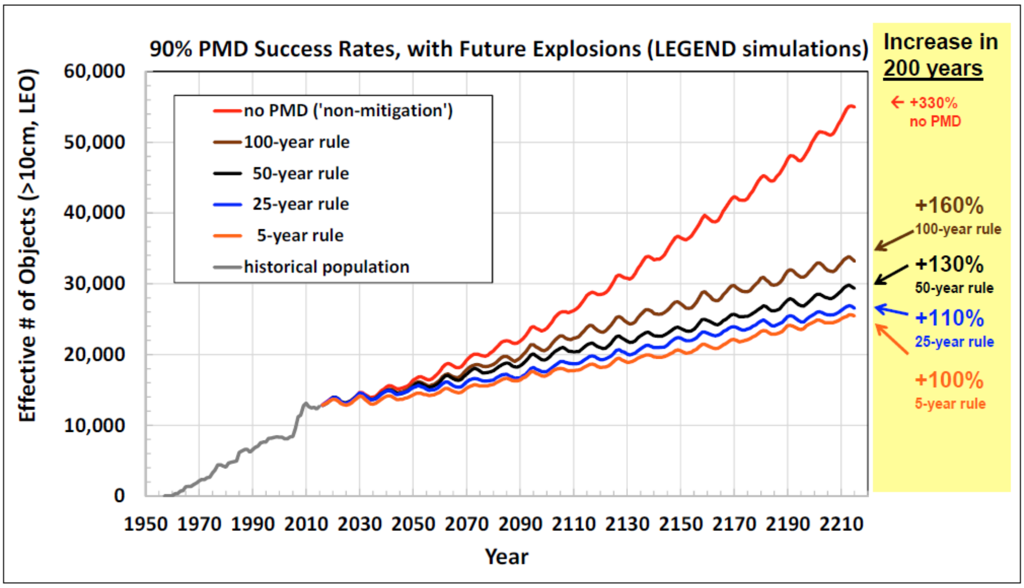

Figure 2. Post Mission Disposal success rates, comparing the 25-year deorbiting rule vs the non-mitigation scenario and other rules [2].

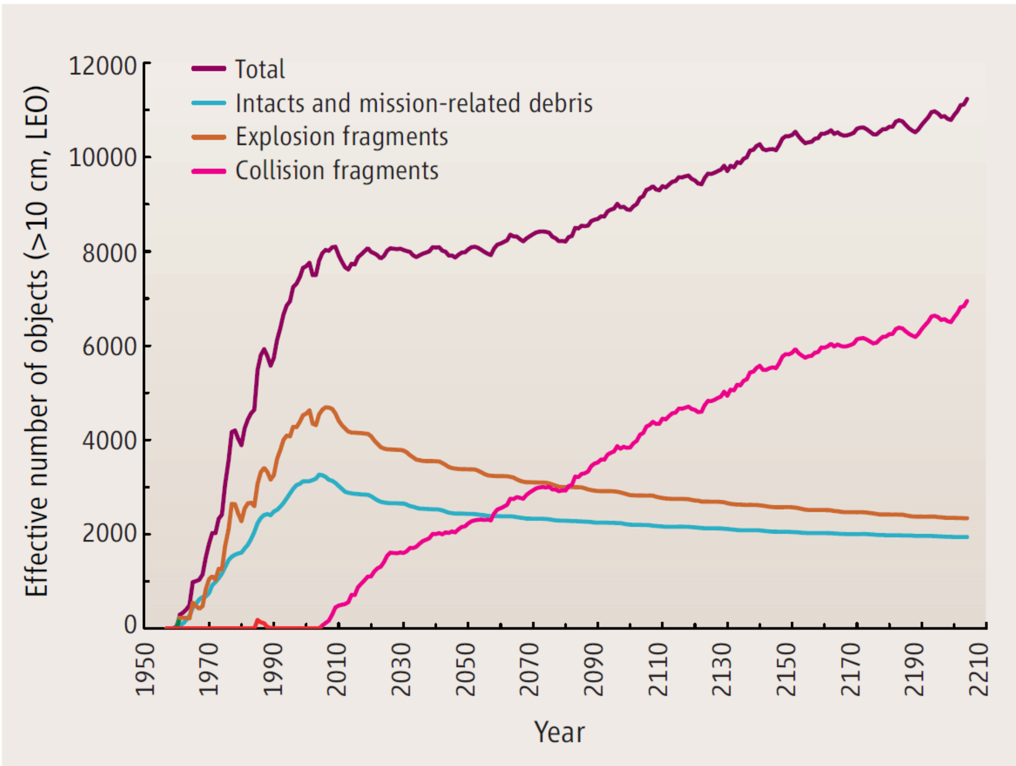

Figure 3. Historical and projected effective number of low Earth orbiting objects greater than 10 cm for orbits between 200 km - 2000 km [7]

901. MEV-2 launched on August 15th 2020, and will service Intelsat 1002. The MEV vehicles have demonstrated docking and life-extension capabilities, which can be directly applied to future active space debris removal missions.

ClearSpace-1 is a technology demonstration satellite mission from ClearSpace SA, which will use a suite of robotic arms to perform rendezvous, capture, and the deorbiting of a Vega Secondary Payload Adapter from the 2013 Vega flight VV02[4]. The contract for this mission was signed in November 2020 by the European Space Agency (ESA) and the mission is set to take place in 2025[5].

Astroscale is a Japanese orbital debris removal company at the forefront of active debris removal technology development. Astroscale was selected for Phase I of the Japan Aerospace Exploration Agency's (JAXA) first debris removal project in February 2020, as the organization seeks to foster the commercialization of space debris removal technologies[6]. Astroscale has also received funding from the Tokyo Metropolitan Government's 'Innovation Tokyo Project' to build out a road map for commercializing active space debris removal services. Most recently, as of March 23rd 2021, Astroscale's End-of-Life Services by Astroscale-demonstration (ELSA-d) satellite has successfully reached orbit[7]. This mission will demonstrate both non-tumbling and tumbling magnetic capture of a target object, and the capability to lose, relocate, approach, and re-capture the target.

The aforementioned companies in the active debris removal and on-orbit servicing markets have begun to demonstrate the commercial and scientific viability of active debris removal technologies. The commercialization of this industry has begun, with over 30 companies who are currently known to be developing systems that are specifically for, or are applicable to, active debris removal.

https://directory.eoportal.org/web/eoportal/satellite-missions/m/mev-1 (accessed 25/03/2021)

[4]'ESA commissions world's first space debris removal', *The European Space Agency*, 2019, https://www.esa.int/Safety_Security/Clean_Space/ESA_commissions_world_s_first_space_debris_removal (accessed 23/03/2021)

[5]'N° 26–2020: Call for Media: ESA and ClearSpace SA sign contract for world's first debris removal mission', *The European Space Agency*, 2020, https://www.esa.int/Newsroom/Press_Releases/Call_for_Media_ESA_and_ClearSpace_SA_sign_contract_for_world_s_first_debris_removal_mission (accessed 23/03/2021)

[6]'Astroscale Selected as Commercial Partner for JAXA's Commercial Removal of Debris Demonstration Project', *Astroscale*, 2020, https://astroscale.com/astroscale-selected-as-commercial-partner-for-jaxas-commercial-removal-of-debris-demonstration-project/ (accessed 23/03/2021)

[7]'Astroscale Celebrates Successful Launch of ELSA-d', *Astroscale*, 2021, https://astroscale.com/astroscale-celebrates-successful-launch-of-elsa-d (accessed 23/03/2021)

1.3. Obruta's Approach to Active Debris Removal

Obruta's approach to active debris removal is through the use of tethered-net technology. Compared to other space-based methods of capture such as the use of robotic arms and end-effectors, tethered-harpoons, electrodynamic tethers, lasers, or magnetism, a tethered-net is capable of capturing a target object regardless of its surface material, surface geometry, or angular rates. It is also scalable for different mission scenarios through the use of a larger or smaller net and/or a longer or shorter tether. Tethered-net capture is already well understood for terrestrial applications, and is quick to be adapted for the orbital environment. For these reasons, ESA shortlisted the tethered-net method as one of two capture methods for their e.Deorbit mission [8] and it was a demonstrated technology during the RemoveDEBRIS mission.

Many net capture simulations [9, 10, 11, 12, 13, 14] and experiments [15, 16, 17, 18, 19] have been performed to model how a net will interact with a target in an orbital environment. Specifically, dynamic models of a net using a lumped-mass model [20, 21], an absolute nodal coordinate formulation (ANCF) model [22, 21], an elastic continuum model [23], and a cubic B-spline mode [24] have been previously discussed.

In focusing on the tether, Obruta team members have previously validated a novel sub-tether configuration for improved target stabilization capabilities during the deployment phase [25] and the post-capture stabilization phase [26]. This tether design with sub-tethers using visco-elastic material properties was first proposed by Hovell and Ulrich [27, 28, 29, 26]. As shown in Fig. 3 this tether configuration is comprised of a single tether spanning from the Servicer spacecraft, denoted as the *main tether*, which branches into several *sub-tethers* at its maximum length, a point denoted as the *junction*, and the sub-tethers are connected to a net at their respective ends.

This tether configuration has an advantage over traditional single-tether configurations in that once the target debris has been ensnared by the net, the viso-elastic properties of the sub-tethers will use the tumbling motion of the target against itself to dampen its angular rates. This dampening effect occurs as long as a tension is maintained on the tether.

Obruta is leveraging the sub-tether configuration and the advantages of nets to develop an active debris removal system that is capable of capturing and deorbiting any orbital object.

[8]European Space Agency, 'ESA's active debris removal mission: e.Deorbit', 2016, [video] https://youtu.be/R6yZLbUCU2c?t=133 (accessed 08/07/2019)

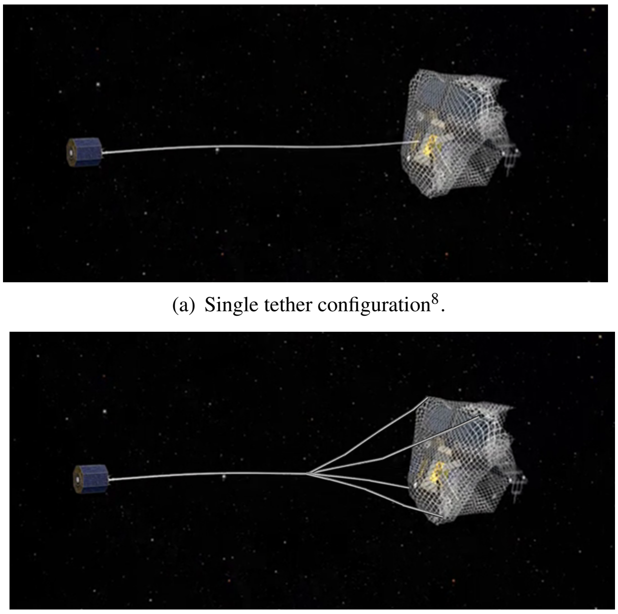

(a) Single tether configuration[8].

(b) Sub-tether configuration [27, 28, 29, 26].

Figure 4. Single- and sub-tether tethered-net configurations.

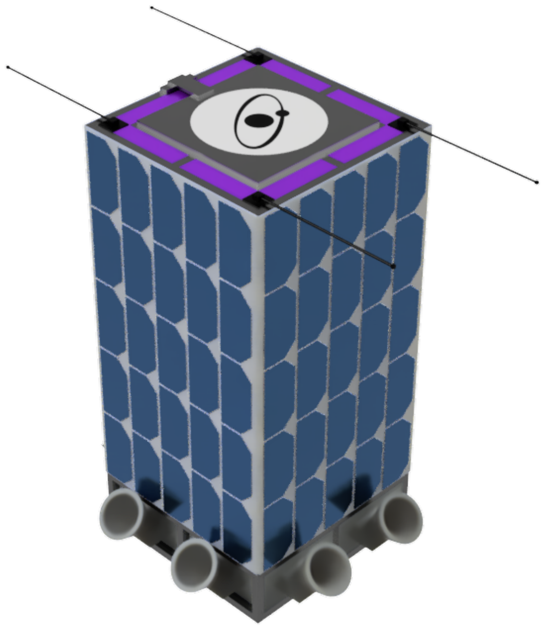

Figure 5. Concept render of an Active Debris Removal System.

2. THE ACTIVE DEBRIS REMOVAL SYSTEM

The Active Debris Removal System (ADRS) is Obruta's active debris removal solution capable of deorbiting any orbital object. Each ADRS contains the necessary subsystems to capture and deorbit an object in a controlled manner. Due to the expendable and high fuel demands of deorbiting orbital objects, the ADRS is intended to be expendable. In order to conserve the resources of the much larger and more capable Servicer spacecraft, the ADRS is to be used as a deployable payload and not a standalone deorbiting system. As such, a Servicer spacecraft carrying a group of ADRSs would be able to deorbit as many orbital objects as it has ADRSs. A concept render of an ADRS is displayed in Fig. 5.

The ADRS has three main subsystem groups: the capture group, the deorbiting group, and the bus. Figure 6 highlights each individual subsystem of the ADRS.

The capture subsystem group located at the zenith section of the ADRS contains a net deployment system that houses the sub-tether configured tethered-net. A deployable hatch covers both of these. A tether reeling mechanism and control system sits below and are responsible for maintaining tension in the tether once the target object has been captured and during the tether reeling process. Located next to the tether control system are an air tank and controller unit. This compressed air is used to deploy the net from the housing unit. Mechanical springs offer an additional approach to tether and net deployment which will be explored by Obruta. In some mission configurations, a vision system containing all necessary sensors required for target location, inspection, and tracking may be outfitted to the ADRS. However, it is preferred to house these sensors on the main Servicer spacecraft.

Located at the nadir section of the ADRS is the deorbiting subsystem group. The ADRS has a single liquid apogee engine located on it's zenith face. Located around the edge of the base are eight attitude thrusters to allow the ADRS control over its attitude while deorbiting a captured object. These attitude control thrusters are also used to dampen any residual rotational motion that a captured object may have after the majority has been stabilized using the sub-tethers. Located above the attitude thrusters are propellant tanks for the liquid propulsion system. These tanks are to be sized according to the target specifications and required final deorbit altitude. For smaller debris objects, reaction wheels or even magnetorquers may be more appropriate choices for ADRS attitude control, and the liquid propulsion deorbiting system may also be substituted for an appropriately sized solid-propellant system or a drag sail at low altitudes. However, for the scenarios explored in this work, a liquid propulsion deorbiting system is required.

Lastly, the bus is the subsystem group that contains all of the necessary hardware to ensure that the ADRS functions and can complete its debris removal mission. Located in between the capture and deorbiting subsystem groups are the electrical power system, communications transmitter and receiver, and on-board computer. All of these subsystems are housed within the overall ADRS structure, which also supports body-mounted solar panels and communications antennas as shown in Fig. 5. Deployable solar panels are preferable for power generation as the captured debris target is often the same size or larger than the ADRS and will often block a significant portion, or all, of the incoming sunlight. To reduce the complexity of the ADRS, body-mounted solar panels are being investigated to determine if they are a viable option based on power requirements of the system.

Due to the aforementioned scalability of a tethered-net, the ADRS is also highly scalable. The fluid tanks and deorbiting subsystem can be appropriately sized to accommodate any target debris object, and the necessary bus subsystems, such as the electrical power system, is also highly scalable. The ADRS can be sized for general classes of debris size and masses, or customized for specific mission scenarios.

2.1. Debris Selection

Obruta is primarily focused on ADRS configurations that are capable of removing the largest and highest-risk debris objects. A coalition of 11 separate teams consisting of members from 13 countries, including the U.S., Russia, China, Japan, and Europe, have previously independently analyzed thousands of orbital debris objects to determine which objects pose the highest risk to operational spacecraft. Their goal was to reach a joint decision on which debris objects pose the biggest risk of creating large amounts of space debris fragments if they were to collide. Each group independently produced what they deemed to be the most dangerous objects before compiling their results into an agreed upon list of the 50 highest risk objects. The rating criteria of the studied debris objects included their chance of collision with other objects, mass, altitude, and several other factors [30].

Of the top 50 highest risk objects, the first 20 listed are all large SL-16 R/B launch vehicle bodies launched by Russia and the Soviet Union (referred to as the Commonwealth of Independent States) between 1987 and 2007. The 21st listed object is Envisat. What was once the worlds largest Earth-observation satellite, Envisat operated for over 10 years before contact was unexpectedly lost and its mission was officially ended[9]. Envisat is chosen as the debris target for determining the deorbiting feasibility of the ADRS as it is a high-risk target, is one of the largest and highest mass debris objects, and it has previously been the study of tethered-net capture [14].

2.2. Mission Profile

The Consortium for Execution of Rendezvous and Servicing Operations (CONFERS) has developed and published a set of baseline mission phases intended to describe the functions of all on-orbit servicing missions [31]. Obruta has adapted these mission phases into a high-level ADRS debris removal mission profile containing six major components:

1. Pre-mission activates, launch, and orbit insertion.
2. On-orbit systems checkout and quiescent parking orbit.
3. Target rendezvous and proximity operations.
4. Target capture and stabilization.
5. Tether reeling and ADRS deployment.
6. Target deorbiting via ADRS and Servicer return to quiescent parking orbit.

Pre-mission activities encompass all deliverables that must be completed before the Servicer spacecraft can be launched into orbit and an ADR mission can begin. This includes assessing the deorbiting needs of the target debris such that an appropriately sized ADRS can be commissioned, establishing service agreements and contracts with all necessary parties, acquiring appropriate licenses, and coordinating mission activities with all relevant parties. Launch and orbit insertion will occur when there is not already an operational Servicer spacecraft with an appropriate ADRS that can access the target debris.

If an active Servicer spacecraft is not available, then a launch will be contracted. Upon arriving in the desired orbit, the Servicer will perform a systems checkout and await an opportunity to rendezvous with the target debris.

Once both parties are ready, the Servicer will rendezvous with the target debris object. Once the rendezvous has been initiated, the Servicer performs orbital transfer and phasing maneuvers to achieve the desired rendezvous and proximity operations (RPO) orbit. The rendezvous ends once the Servicer has achieved the outer limits of a predefined proximity operations control volume. From this position, proximity operations such as pre-servicing inspections of the target debris can take place.

Once the Servicer is ready to proceed with deorbiting operations it will incrementally maneuver towards the target debris until it rests at a final position lagging behind and appropriately spaced from the target to optimize the net deployment and capture. From this position the ADRS net and tether deployment mechanism cover will open and the net will be deployed by launching four weighted corner bullets attached to the net. The net will unfurl during flight and will wrap around the target debris upon contact. A net-closing mechanism such as the method proposed by Shan [14] may be used to ensure the debris does not become untangled from the net. Once ensnared, the Servicer will begin to thrust opposite the direction of flight of the tethered debris in order to maintain tension in the main and sub-tethers. As the captured debris tumbles it will continually stretch against the visco-elastic subtethers which will dampen its rotational motion over time.

[9]'Envisat', *The European Space Agency*, https://earth.esa.int/eogateway/missions/envisat (accessed 18/02/2021)

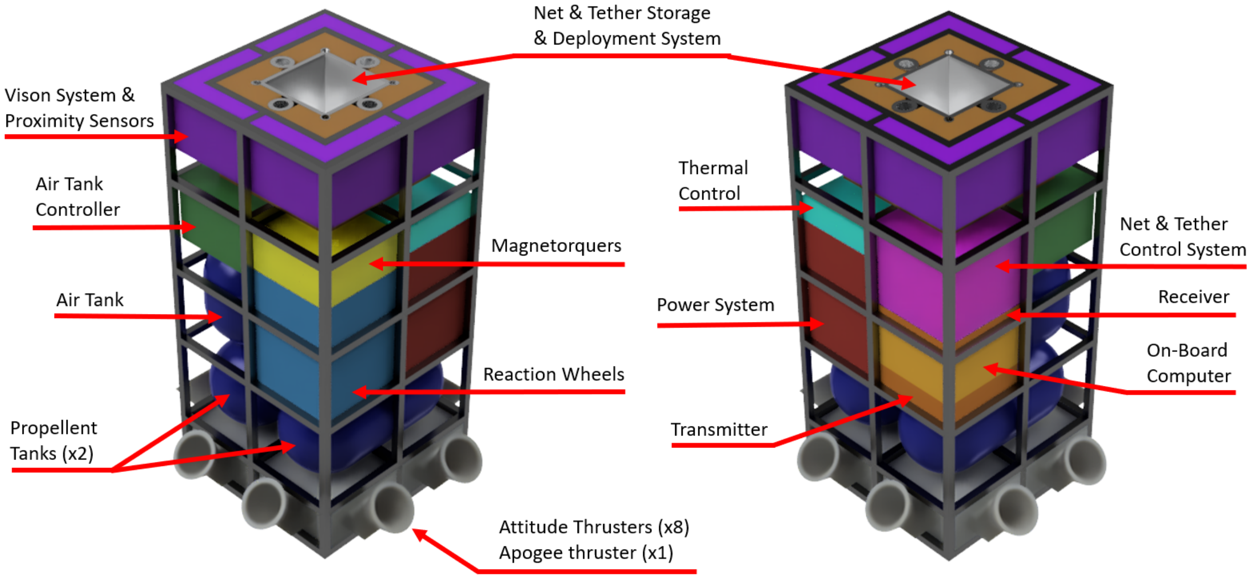

Figure 6. ADRS components breakdown.

Once the targets angular rates are sufficiently reduced, the tether will be reeled into the ADRS. Once completely reeled in it will effectively create a rigid connection between the ADRS and the captured target. From this position, the Servicer will deploy the ADRS and back away from the now pseudo-rigidly connected ADRS and debris system. The ADRS will then have full control over the deorbiting mission from this point on.

Lastly, once the ADRS has been deployed and the Servicer is sufficiently clear of the ADRS-debris system, the ADRS can begin a deorbiting burn to reduce the debris' altitude, or if in geostationary orbit, maneuver it to a graveyard orbit. Dependant on the mission requirements, the ADRS can lower the altitude of the debris until it is in a position to naturally deorbit within a specified amount of time, or the ADRS can completely lower the debris until both burn up upon atmospheric reentry. The Servicer is then free to return to a quiescent parking orbit and await further deorbiting missions if carrying more ADRS payloads, or to continue performing inspection services if it is not longer carrying any ADRS payloads.

3. NUMERICAL SIMULATIONS

Numerical simulations are useful for initially understanding how a tether can be deployed, a target can be stabilized, and how an ADRS can deorbit an object in an orbital environment. By modeling the dynamics of a Servicer spacecraft/ADRS, a tether, and a debris object, and including perturbations present in the orbital environment, the viability of an active debris removal mission scenario using an ADRS can be investigated. This section presents the dynamical motion of a Servicer spacecraft/ADRS, a tether, and a debris object. It brings the sub-tether deployment work of Stadnyk and Ulrich [25], builds upon the post-capture sub-tether stabilization work from Hovell and Ulrich [26], explores the dynamics of a tethered Servicer and debris object when reeling in the tether, and investigates the deorbiting potential of a connected ADRS-debris system to demonstrate a complete capture scenario using an ADRS.

3.1. Model Reference Frame

In this work, when modeling the orbital environment of the Servicer spacecraft, ADRS, tethers, and debris object (Envisat), $\mathcal{F}_{\mathrm{I}}$ represents an inertially-fixed reference frame. The position of the debris is described by the vector $\vec{r}_{\mathrm{t}}$. These are used to calculate the three-dimensional components of the debris center of mass position vector in the inertially fixed reference frame, represented as $\mathbf{r}_{\mathrm{t}}$

$$\vec{r}_{\mathrm{t}} = \vec{\mathcal{F}}_{\mathrm{I}}^{\mathrm{T}} \mathbf{r}_{\mathrm{t}} \tag{1}$$

The Servicer/ADRS, and tether nodes are represented as point masses. Their locations are respectively described by position vectors $\vec{r}_{\mathrm{C}}$ and $\vec{r}_{\mathrm{n}_i}$, respectively, such that

$$\vec{r}_{\mathrm{C}} = \vec{\mathcal{F}}_{\mathrm{I}}^{\mathrm{T}} \mathbf{r}_{\mathrm{C}} \tag{2}$$

$$\vec{r}_{\mathrm{n}_i} = \vec{\mathcal{F}}_{\mathrm{I}}^{\mathrm{T}} \mathbf{r}_{\mathrm{n}_i} \tag{3}$$

where $\mathbf{r}_{\mathrm{C}}$ and $\mathbf{r}_{\mathrm{n}_i}$ are the three-dimensional components of the Servicer and i^{th} node position vectors in the inertially fixed reference frame, respectively.

3.2. Attitude Motion

Euler's equations of motion are used to describe the target debris angular rates in the body-fixed reference frame $\mathcal{F}_\mathrm{B}$ [32]. This is given by

$$\mathbf{J}\dot{\boldsymbol{\omega}} + \boldsymbol{\omega}^\times(\mathbf{J}\boldsymbol{\omega}) = \boldsymbol{\tau} \tag{4}$$

where $\mathbf{J}$ is the inertia matrix of the debris, $\boldsymbol{\omega}$ is the components of the angular rate vector in $\mathcal{F}_\mathrm{B}$, and $\boldsymbol{\tau}$ is the sum of all external torques applied to the debris.

It is assumed that $\mathcal{F}_\mathrm{B}$ is aligned with the principal axes of the body. Therefor $\mathbf{J}$ can be simplified to

$$\mathbf{J} = \begin{bmatrix} J_{xx} & 0 & 0 \\ 0 & J_{yy} & 0 \\ 0 & 0 & J_{zz} \end{bmatrix} \tag{5}$$

where J_{xx}, J_{yy}, and J_{zz} are the principal moments of inertia of the debris.

The debris attitude is described using quaternion kinematics [32]

$$\dot{\mathbf{q}} = \frac{1}{2}\begin{bmatrix} \left(\boldsymbol{\epsilon}^\times + \eta\mathbf{I}_{3\times3}\right)\boldsymbol{\omega} \\ -\boldsymbol{\epsilon}^\mathrm{T}\boldsymbol{\omega} \end{bmatrix} \tag{6}$$

where $\mathbf{q}$ represents the attitude quaternion in $\mathcal{F}_\mathrm{B}$ with respect to the inertially-fixed reference frame, $\mathcal{F}_\mathrm{I}$. It is defined as

$$\mathbf{q} = \begin{bmatrix} q_1 \\ q_2 \\ q_3 \\ q_4 \end{bmatrix} = \begin{bmatrix} \boldsymbol{\epsilon} \\ \eta \end{bmatrix} = \begin{bmatrix} \mathbf{b}\cos(\frac{\phi}{2}) \\ \sin(\frac{\phi}{2}) \end{bmatrix} \tag{7}$$

where $\mathbf{b}$ is the axis of rotation, ϕ is the angle of rotation, and

$$\boldsymbol{\epsilon} = \begin{bmatrix} q_1 \\ q_2 \\ q_3 \end{bmatrix} \tag{8}$$

$$\eta = q_4. \tag{9}$$

A perturbation affecting the debris attitude is introduced into the simulated environment. The gravity-gradient torque, which is due to the inverse square law of the gravitational field of the Earth, causes an unequal gravitational force acting across the debris body and leads to restoring torques to acting on it [32]. This effect is quantified through

$$\boldsymbol{\tau}_\mathrm{g} = \frac{3\mu}{\|\mathbf{r}_\mathrm{t}^\mathrm{b}\|^5}\mathbf{r}_\mathrm{t}^{\mathrm{b}\times}\mathbf{J}\mathbf{r}_\mathrm{t}^\mathrm{b} \tag{10}$$

where $\boldsymbol{\tau}_\mathrm{g}$ is the resulting gravity-gradient torque components in $\mathcal{F}_\mathrm{B}$, μ is the gravitational parameter of the Earth, and $\mathbf{r}_\mathrm{t}^\mathrm{b}$ are the components of the debris position vector expressed in $\mathcal{F}_\mathrm{B}$, as

$$\mathbf{r}_\mathrm{t}^\mathrm{b} = \mathbf{C}_\mathrm{BI}(\mathbf{q})\mathbf{r}_\mathrm{t} \tag{11}$$

where the rotation matrix $\mathbf{C}_\mathrm{BI}(\mathbf{q})$ denotes a rotation from $\mathcal{F}_\mathrm{I}$ to $\mathcal{F}_\mathrm{B}$. This is obtained from the quaternion $\mathbf{q}$ by

$$\mathbf{C}_\mathrm{BI}(\mathbf{q}) = \begin{bmatrix} 1-2q_2^2-2q_3^2 & 2(q_1q_2+q_4q_3) & 2(q_1q_3-q_4q_2) \\ 2(q_1q_2-q_4q_3) & 1-2q_1^2-2q_3^2 & 2(q_2q_3+q_4q_1) \\ 2(q_1q_3+q_4q_2) & 2(q_2q_3-q_4q_1) & 1-2q_1^2-2q_2^2 \end{bmatrix} \tag{12}$$

3.3. Translational Motion

Newton's second law is used to model the linear motion of the Servicer spacecraft/ADRS, tether nodes, and debris

$$\mathbf{F} = m\ddot{\mathbf{r}} \tag{13}$$

where $\mathbf{F}$ is the components of the net force applied to the body, m is the mass of the body in question, and $\ddot{\mathbf{r}}$ is the inertial linear acceleration.

The force due to gravity acting on a body, $\mathbf{F}_\mathrm{g}$, is described by Newton's law of gravitation

$$\mathbf{F}_\mathrm{g} = -\frac{\mu m}{\|\mathbf{r}\|^3}\mathbf{r} \tag{14}$$

where $\mathbf{r}$ is the components of the position vector of the orbiting spacecraft or tether node in $\mathcal{F}_\mathrm{I}$.

The aerodynamic drag translational perturbation is included in the simulator. The aerodynamic force on a body is given by

$$\mathbf{F}_\mathrm{d} = \frac{1}{2}C_\mathrm{d}A\rho\dot{\mathbf{r}}^2 \tag{15}$$

where C_d is the drag coefficient, A is the cross-sectional area, ρ is the atmospheric density, and $\dot{\mathbf{r}}$ is the relative velocity between the spacecraft and the atmosphere. The NRLMSISE-00 atmospheric density model is used [33].

3.4. Tether Deployment Model

During tether deployment, the tether is approximated as a series of lumped mass nodes connected by massless spring-damper elements. Force acting on the i^th node generated by the j^th node connected to it is calculated as

$$F_{ij} = -k(r_{ij} - L_0) - c\dot{r}_{ij} \tag{16}$$

where k is the axial stiffness, c is the damping coefficient, L_0 is the unstretched length of the tether segment between the i^{th} and j^{th} nodes, and r_{ij} and $\dot{r}_{ij}$ are the respective relative positions and velocities between the i^{th} and j^{th} tether nodes.

The tether is assumed to be constructed from a homogeneous isotropic linear material. Therefore the axial stiffness of the tether is defined as

$$k = \frac{EA}{L_0} \tag{17}$$

where E is the elastic Young's modulus of the tether material and A is the cross-sectional area of the tether.

The damping coefficient is dependent on the tether material. It is calculated as

$$c = 2\zeta\sqrt{m_i k} \tag{18}$$

where ζ is the damping ratio and m_i is the mass of node i.

The lumped mass distribution of each node is modeled as the half-masses of the number of adjacent nodes and the cross-sectional area of each tether segment to any given node. The tether has three distinct node masses, with the mass of the i^{th} node determined by the conditions

$$m_i = \begin{cases} m_{\text{bullet}}, & \text{for } i \text{ at the tether end} \\ \rho A l_0, & \text{for } i \text{ along the tether} \\ \frac{3}{2}\rho A L_0, & \text{for } i \text{ at the tether junction} \end{cases} \tag{19}$$

where ρ is the material density of the tether.

A tension force is only generated when the element is elongated, and elements of the tether are not able to withstand compression. These two considerations give the applied force conditions of

$$\mathbf{F}_{ij} = \begin{cases} F_{ij}\frac{\mathbf{r}_{ij}}{||\mathbf{r}_{ij}||}, & \text{for } r_{ij} > L_0 \\ 0, & \text{otherwise.} \end{cases} \tag{20}$$

3.5. Post-Capture Tether Model

The tethers during the post-capture stabilization phase are modeled as a single massless spring-damper element between the spacecraft body and junction as done by Hovell and Ulrich's [26]. Torsion and bending effects are again ignored in the tether. Forces generated by a tether element are only generated while that element is in tension and the forces are applied to each connected mass.

The i^{th} sub-tether under analysis by the vector $\vec{L}_i$, in $\mathcal{F}_{\text{I}}$ has components of

$$\mathbf{L}_i = \mathbf{r}_{n_i} - \mathbf{r}_t - \mathbf{C}_{\text{BI}}(\mathbf{q})^{\text{T}}\chi_{\text{t},i}, \qquad \forall\, i = 1, ..., 4 \tag{21}$$

where $\chi_{\text{t},i}$ is the attachment point of the i^{th} sub-tether relative to the center of mass of the debris in $\mathcal{F}_{\text{B}}$.

The linear spring and damper are treated in parallel, the resultant tensile force magnitude developed by the i^{th} sub-tether is

$$F_i = \begin{cases} k(\|\mathbf{L}_i\| - L_0) + c[\dot{\mathbf{r}}_{\text{n}_i} - (\dot{\mathbf{r}}_{\text{t}} + \\ \mathbf{C}_{\text{BI}}(\mathbf{q})^{\text{T}}\boldsymbol{\omega}^{\times}\chi_i)]^{\text{T}}\frac{\mathbf{L}_i}{\|\mathbf{L}_i\|}, & \text{for } \|\mathbf{L}_i\| - L_0 > 0 \\ 0, & \text{otherwise} \end{cases} \tag{22}$$

where $\dot{\mathbf{r}}_{\text{t}}$ and $\dot{\mathbf{r}}_{\text{n}_i}$ are the velocity components of the debris and junction point in $\mathcal{F}_{\text{I}}$, respectively. Tether elements are assumed to have a constant spring constant, k, and damping coefficient, c, and are calculated the same as Eq. (17) and (18), respectively.

3.6. Equations of Motion

The equations of motion of the Servicer spacecraft/ADRS, debris, and tether nodes can be broken down into four phases: deployment of the tether, the post-capture stabilization of the tethered system, the reeling in of the tether, and the deorbiting of the ADRS-debris system.

Due to the assumption that the Servicer/ADRS and tether nodes modeled as point masses, attitude motion is only modeled for the debris. Torque imparted on the debris is calculated as the sum of the gravity-gradient effects defined in $\mathcal{F}_{\text{B}}$, the four sub-tether contributions, and attitude control thrust applied by the ADRS.

$$\boldsymbol{\tau}_{\text{t}} = \boldsymbol{\tau}_{\text{g}} + \boldsymbol{\tau}_{\text{s}} + \boldsymbol{\tau}_{\text{thrust}} = \\ \frac{3\mu}{\|\mathbf{r}_t^{\text{b}}\|^5}\mathbf{r}_{\text{t}}^{\text{b}\times}\mathbf{J}\mathbf{r}_{\text{t}}^{\text{b}} + \mathbf{C}_{\text{BI}}(\mathbf{q})\sum_{i=1}^{4} F_i\frac{\mathbf{a}_i^{\times}\mathbf{L}_i}{\|\mathbf{L}_i\|} + F_{\text{thrust}}\boldsymbol{l} \tag{23}$$

where $\boldsymbol{l}$ is the components of the length of the moment arm from the ADRS-debris system center of mass to the ADRS.

Torque on the debris follows these conditions during each of the four phases

$$\boldsymbol{\tau}_{\text{t}} = \begin{cases} \boldsymbol{\tau}_{\text{s}} = \boldsymbol{\tau}_{\text{thrust}} = 0, & \text{during tether deployment} \\ \boldsymbol{\tau}_{\text{thrust}} = 0, & \text{during stabilization} \\ \boldsymbol{\tau}_{\text{thrust}} = 0, & \text{during tether reeling} \\ \boldsymbol{\tau}_{\text{s}} = 0, & \text{during deorbiting.} \end{cases} \tag{24}$$

Translational motion affecting the debris is a combination of the gravitational effects from Earth, aerodynamic drag, forces imparted by sub-tethers in tension, and forces imparted by the ADRS during deorbiting. It is expressed in $\mathcal{F}_I$ as

$$m_{\mathrm{t}}\frac{\mathrm{d}\dot{\mathbf{r}}_{\mathrm{t}}}{\mathrm{d}t} = \mathbf{F}_{\mathrm{t}} = \mathbf{F}_{\mathrm{g}} + \mathbf{F}_{\mathrm{d}} + \mathbf{F}_{\mathrm{s}} + \mathbf{F}_{\mathrm{thrust}} = \\ -\frac{\mu m_{\mathrm{t}}}{\|\mathbf{r}_{\mathrm{t}}\|^3}\mathbf{r}_{\mathrm{t}} + \frac{1}{2}C_{\mathrm{d}}A\rho\dot{\mathbf{r}}_{\mathrm{t}}^2 + \sum_{i=1}^{4} F_i\frac{\mathbf{L}_i}{\|\mathbf{L}_i\|} + \\ F_{\mathrm{thrust}}\frac{\dot{\mathbf{r}}_{\mathrm{ADRS}}}{\|\dot{\mathbf{r}}_{\mathrm{ADRS}}\|} \quad (25)$$

Translational forces affecting the debris follow these conditions during each of the four phases

$$\mathbf{F}_{\mathrm{t}} = \begin{cases} \mathbf{F}_{\mathrm{s}} = \boldsymbol{F}_{\mathrm{thrust}} = 0, & \text{during tether deployment} \\ \mathbf{F}_{\mathrm{thrust}} = 0, & \text{during stabilization} \\ \mathbf{F}_{\mathrm{thrust}} = 0, & \text{during tether reeling} \\ \mathbf{F}_{\mathrm{s}} = 0, & \text{during deorbiting.} \end{cases} \quad (26)$$

The Servicer spacecraft/ADRS is affected by gravitational effects, an approximated aerodynamic drag force, tension in the main tether, a thrust force during deorbiting, and an instantaneous impulse force at the time of tether deployment. Forces on the Servicer/ADRS are expressed as

$$m_{\mathrm{c}}\frac{\mathrm{d}\dot{\mathbf{r}}_{\mathrm{c}}}{\mathrm{d}t} = \mathbf{F}_{\mathrm{c}} = \mathbf{F}_{\mathrm{g}} + \mathbf{F}_{\mathrm{d}} + \mathbf{F}_{\mathrm{m}} + \mathbf{F}_{\mathrm{impulse}} + \mathbf{F}_{\mathrm{thrust}} = \\ -\frac{\mu m_{\mathrm{c}}}{\|\mathbf{r}_{\mathrm{c}}\|^3}\mathbf{r}_{\mathrm{c}} + \frac{1}{2}C_{\mathrm{d}}A\rho\dot{\mathbf{r}}_{\mathrm{c}}^2 + -F_m\frac{\mathbf{L}_m}{\|\mathbf{L}_m\|} + \\ \sum_{i=1}^{4} F_{\mathrm{impulse}_i}\frac{\mathbf{r}_{\mathrm{b}}}{\|\mathbf{r}_{\mathrm{b}}\|} + F_{\mathrm{thrust}}\frac{\dot{\mathbf{r}}_{\mathrm{ADRS}}}{\|\dot{\mathbf{r}}_{\mathrm{ADRS}}\|} \quad (27)$$

Translational forces affecting the Servicer spacecraft/ADRS follow these conditions

$$\mathbf{F}_{\mathrm{c}} = \begin{cases} \mathbf{F}_{\mathrm{thrust}} = 0, & \text{during tether deployment} \\ \mathbf{F}_{\mathrm{impulse}} = 0, & \text{during stabilization} \\ \mathbf{F}_{\mathrm{impulse}} = 0, & \text{during tether reeling} \\ \mathbf{F}_{\mathrm{m}} = \mathbf{F}_{\mathrm{impulse}} = 0, & \text{during deorbiting.} \end{cases} \quad (28)$$

During tether deployment translational forces affecting a given tether node, denoted by the subscript i, experiences similar forces to the Servicer spacecraft/ADRS. A bullet node will experience an additional one-time impulse force when deployed. These forces are given by the conditions in Eq. (30), where the subscript 's' denotes the sub-tether, and 'm' denotes the main tether.

During post-capture stabilization, only the junction node is modeled. The translational forces experienced by this node are expressed as

$$m_{\mathrm{j}}\frac{\mathrm{d}\dot{\mathbf{r}}_{\mathrm{j}}}{\mathrm{d}t} = \mathbf{F}_{\mathrm{j}} = \mathbf{F}_{\mathrm{m}} - \mathbf{F}_{\mathrm{s}} + \mathbf{F}_{\mathrm{g}} = \\ F_{\mathrm{m}}\frac{\mathbf{L}_{\mathrm{m}}}{\|\mathbf{L}_{\mathrm{m}}\|} - \sum_{i=1}^{4} F_i\frac{\mathbf{L}_i}{\|\mathbf{L}_i\|} - \frac{\mu m_{\mathrm{j}}}{\|\mathbf{r}_{\mathrm{j}}\|^3}\mathbf{r}_{\mathrm{j}} \quad (29)$$

In summary, to simulate the dynamics, Eqs. (23) to (30) are solved numerically with Eqs. (4) and (13) and the conditions outlined in this section.

4. ACTIVE DEBRIS REMOVAL MISSION SIMULATION RESULTS

The equations of motion and tether numerical models presented in Sec. 3 are used to create a complete end-to-end ARDS-enabled active debris removal mission simulation. The simulation methods previously employed to investigate sub-tether deployment and post-capture stabilization dynamics [26, 25] are built upon to determine the feasibility of the ADRS in an appropriate mission-like environment—one which cannot be easily recreated under laboratory conditions. A net has been omitted from the simulation to reduce the complexity of the mission scenario.

The debris is modeled as a rectangular prism while the Servicer and tether nodes are modelled as point masses to reduce complexity. Two-body motion is assumed, and the implemented aerodynamic drag perturbation is assumed to have no effect on the debris attitude. Two separate simulations are performed: 1) the tether is deployed, the debris is stabilized, and the debris is deorbited; 2) the tether is deployed, the debris is stabilized, the tether is reeled in, and the debris is deorbited. Each subsection will focus on one aspect of this capture-detumble-deorbit scenario.

Envisat was selected as the debris to deorbit. The approximate orbital elements of Envisat are shown in Table 1 and its mass properties are shown in Table 2.

$$m_{\mathrm{n}_i}\frac{\mathrm{d}\dot{\mathbf{r}}_{\mathrm{n}_i}}{\mathrm{d}t} = \mathbf{F}_{\mathrm{n}_i} = \begin{cases} \mathbf{F}_{\mathrm{c}}, & \text{when } i \text{ is attached to the chaser} \\ \mathbf{F}_{\mathrm{g}_i} + \mathbf{F}_{ii+1} + \mathbf{F}_{ii-1}, & \text{when } i \text{ is in flight} \\ \mathbf{F}_{\mathrm{g}_i} + \sum\limits_{k=1}^{4} \mathbf{F}_{i\mathrm{s}_{k_1}} + \mathbf{F}_{i\mathrm{m}_{\mathrm{end}}}, & \text{when } i \text{ is the junction node in flight} \\ \mathbf{F}_{\mathrm{g}_i} + \mathbf{F}_{ii-1} + \mathbf{F}_{\mathrm{impulse}}, & \text{when } i \text{ is a bullet node in flight} \end{cases} \quad (30)$$

Table 1. Envisat orbital elements[10].

Orbital Element	Value
Semi-major axis, a	7143 km
Eccentricity, e	0.00014
Right ascension of the ascending node, Ω	84.4 deg
Inclination, i	98.1 deg
Argument of perigee, ω	91.1 deg
True anomaly, θ_t	60 deg

Table 2. Mass properties of Envisat and the ADRS system and tether properties.

Parameter	Value	Parameter	Value
Debris Size, m	[5,10,5]	m_t, kg	8211
J_{xx}, $\mathrm{kg \cdot m^2}$	124,800	m_c, kg	500
J_{yy}, $\mathrm{kg \cdot m^2}$	17,000	m_j, kg	10
J_{zz}, $\mathrm{kg \cdot m^2}$	129,100	m_b, kg	5
L_{main}, m	15.0	m_n, kg	1
L_{sub}, m	15.2	k, $\frac{\mathrm{N}}{\mathrm{m}}$	3150
A, $\mathrm{m^2}$	50	c, $\frac{\mathrm{Ns}}{\mathrm{m}}$	16
C_d	2		

4.1. Tether Deployment

This subsection presents the tether deployment simulation. The initial conditions of the debris are calculated using the orbital elements found in Table 1. The initial position and velocity vectors of the chaser spacecraft are similarly calculated, however, its position trails the debris by 30 m in the flight direction. All orbital elements between the chaser and target debris are the same, with the exception of the chaser's true anomaly given as

$$\theta_c = \theta_t - \frac{30}{\|\mathbf{R}_{I_t}\|}. \tag{31}$$

The simulations are performed using an Adams integration scheme over 370 seconds with a 0.1 second time step. The tether bullets are deployed each at 0.08 m/s with an angle of 4° from the chaser's velocity vector such that the bullets expand and capture the debris at its extremities. The debris has an initial attitude of $q = [-0.6312, 0.4152, -0.5797, 0.3050]$ and initial angular rate is $\omega = [0.005, 0.005, 0.0166]$ rad/s. The bullet mass is m_{b}, each of the 5 tether nodes has a mass of m_{n}, and the tether junction has a mass of m_{j}, as listed in Table 2.

Snapshots of the simulated tether deployment are shown in Fig. 7.

[10] Obtained from https://www.n2yo.com/satellite/?s=27386 (accessed 28/03/2021)

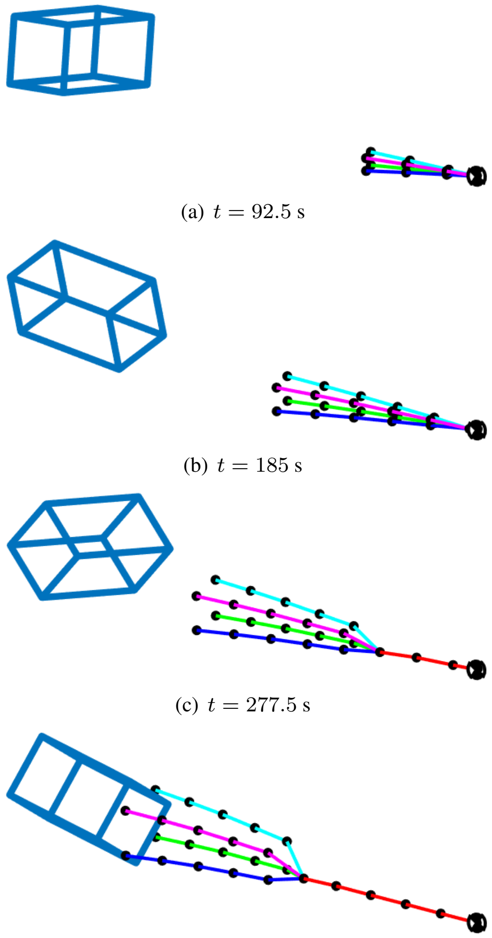

(a) $t = 92.5$ s

(b) $t = 185$ s

(c) $t = 277.5$ s

(d) $t = 370$ s

Figure 7. Snapshots of tether deployment.

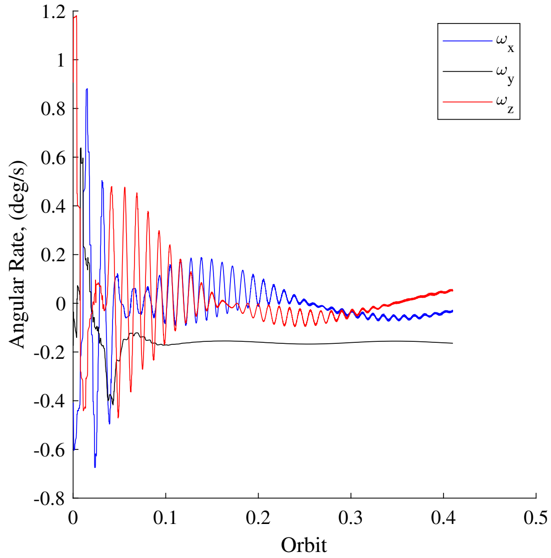

Figure 8. Target angular rates during stabilization.

The tether deployment is successful. When the bullets contact the debris, they are assumed to rigidly connect to the debris. With the tethers rigidly attached to the debris, the tether stabilization phase can begin, as presented in the following subsection.

4.2. Debris Stabilization

With the tethers rigidly attached to the debris, the stabilization phase of the capture-stabilize-deorbit system can begin. The sub-tether configuration was chosen because it is known to aid in the stabilization of the debris [26]. Here, a retrograde continuous thrust of $F_{\text{thrust}} = 20$ N was used by the chaser. This causes the chaser to maintain tension on the tether which, over time, will stabilize the debris due to the tether damping. In order to prevent chaser transverse motion, a simple derivative controller is used to keep the relative velocity between the chaser and debris equal to zero. The bullets are attached to the extremities of the debris, and the debris initially has the same angular rates of $\omega = [0.005, 0.005, 0.0166]$ rad/s. All other tether configuration parameters are identical to the final parameters of Sec. 4.1. The stabilization simulation is performed over 3004 seconds (1/2 an orbit) at a 1 second time step. The goal is to safely reduce the angular rates of the debris over time, which is shown in Fig. 8.

The angular rates decrease over time, indicating that the stabilization phase is successful. The angular rates about the x and z axis oscillate around 0 at their orbital period, but the y axis angular rate is nonzero. This indicates that the angular velocity along the tether axis is uncontrolled with a tethered spacecraft system. Future investigation should be done to determine whether a single-axis spin is 1) a problem; 2) can be controlled with another technique. Now that the debris is stabilized, it can either be a) deorbited; or b) the tether can be reeled in before deorbiting. The following subsection presents the tether reeling.

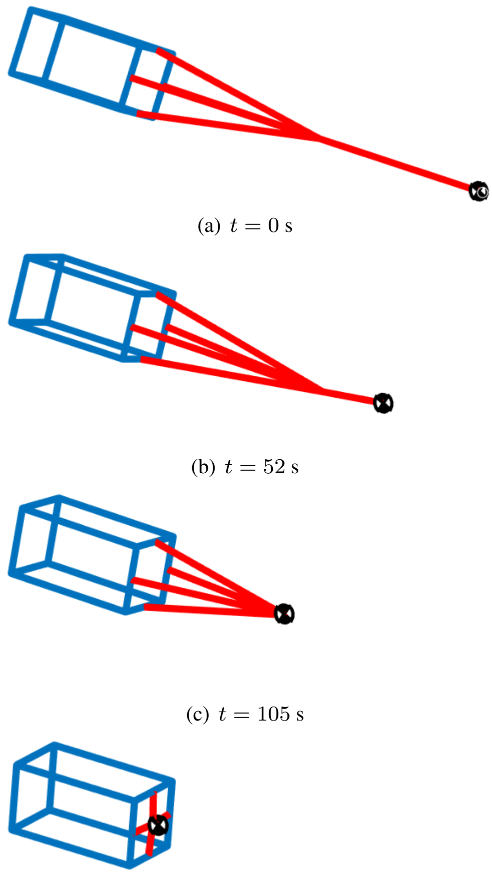

(a) $t = 0$ s

(b) $t = 52$ s

(c) $t = 105$ s

(d) $t = 157$ s

Figure 9. Snapshots of tether reeling.

4.3. Tether Reeling

From the stabilized state obtained after the simulation in Sec. 4.2, the variation where the tether is reeled in is investigated next. To simulate the tether reeling mechanism, the unstretched length of the main tether is reduced at 0.176 m/s for the first 80 seconds. Following this, the sub-tether unstretched lengths are reduced at 0.189 m/s for the next 80 seconds. The simulation is performed over 157 s with a time step of 0.1 s. Snapshots of the tether reeling are shown in Fig. 9

The tether was successfully reeled. It is assumed that the chaser creates a rigid connection with the debris to aid with deorbiting.

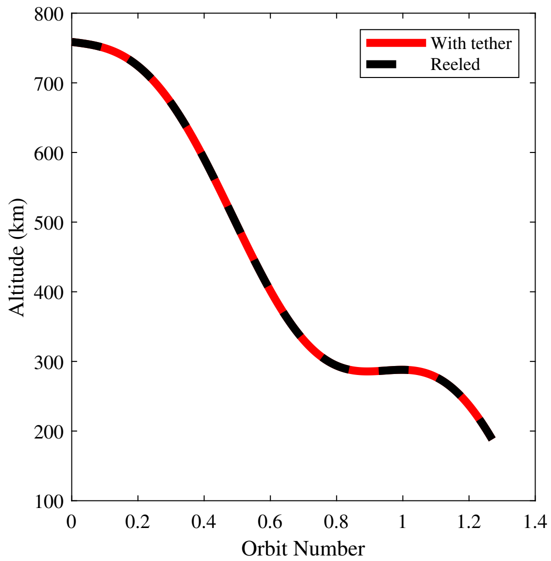

Figure 10. Altitude over time.

4.4. Deorbiting

This subsection studies the deorbiting of the chaser-debris combination. It considers deorbiting both with and without the tether in the reeled state. In other words, it considers deorbiting both using the conditions at the end of Sec. 4.2 and Sec. 4.3. In both cases, a continuous deorbiting thrust of 400 N was used. The simulation was run for 7,800 s (1.3 orbits) at a time step of 1 s. A plot of the altitude as a function of time is shown in Fig. 10.

Both deorbiting configurations—using the tether and with the tether reeled—yield identical altitude plots over time. The impulse needed to remove altitude from the orbit is independent of deorbiting configuration. However, being rigidly attached to the debris may have control benefits and should be studied further.

To approximate the fuel burn needed to reduce the altitude, the equation for I_{sp}

$$I_{\text{sp}} = \frac{F}{\dot{m} g_0} \tag{32}$$

can be integrated, assuming a constant force F and I_{sp} to obtain

$$\Delta m = \frac{F \Delta t}{I_{\text{sp}} g_0} \tag{33}$$

where Δm is the amount of fuel required for this non-impulsive deorbiting manoeuvre. Assuming an I_{sp} of 321 s, Eq. (33) was used to plot the fuel needed to bring Envisat to a variety of final altitudes, shown in Fig. 11.

The amount of fuel needed to deorbit Envisat is significant. Though, fuel savings can be realized by instead bringing Envisat to a higher-altitude orbit where it will more rapidly deorbit on its own.

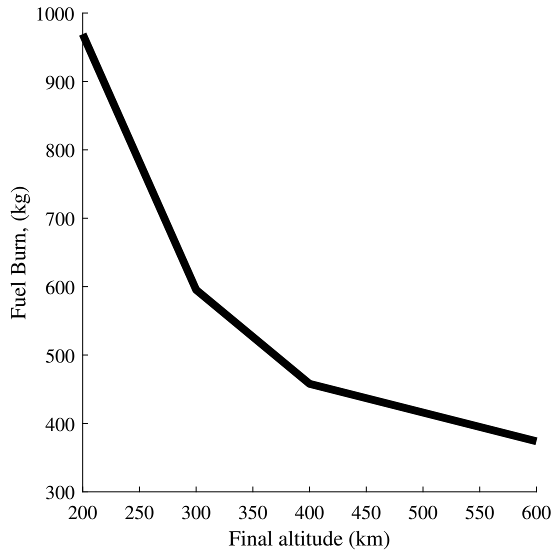

Figure 11. Fuel burn vs final altitude.

5. CONCLUSION

The concept of Obruta's Active Debris Removal System was presented and found to be a feasible approach to deorbiting an orbital object. Specifically, the feasibility of deorbiting an approximation of the defunct satellite Envisat was investigated. Two active debris removal mission scenarios were investigated, both through the use of a tethered-net with a sub-tether configuration to first capture the and stabilize the debris, then deorbiting by towing the tethered object to a lower altitude orbit, or by reeling in the tether in order to create a rigid connection and maintain a higher degree of control over the debris object while it is towed to a lower altitude. It is concluded that reeling in the tether to the ADRS is a superior approach, as the debris is observed to exhibit uncontrollable rotational motion about the ADRS-debris tethered axis while being towed via an elongated tether, and the higher degree of control that the ADRS maintains with a rigid connection when the tether is reeled in results in less required attitude correcting maneuvers and a lower overall fuel requirement for the deorbiting mission.

ACKNOWLEDGMENTS

Obruta Space Solutions acknowledges the support of the Canadian Space Agency (CSA) [20STDPM01] in their contributions helping fund this research.

REFERENCES

1. Kessler, D. J. and Cour-Palais, B. G., “Collision Frequency of Artificial Satellites: The Creation of a Debris Belt,” *Journal of Geophysical Research*, Vol. 83, No. A6, 1978, pp. 2637–2646.

2. "Orbital Debris Quarterly News," *NASA Orbital Debris Program Office*, Vol. 24, No. 1, 2020.
3. Pardini, C. and Anselmo, L., "Assessment of the Consequences of the Fengyun-1C Breakup in Low Earth Orbit," *Advances in Space Research*, Vol. 44, No. 5, 2009, pp. 545–557.
4. Kelso, T. S., "Analysis of the Iridium 33-Cosmos 2251 Collision," Tech. rep., 2009.
5. Crowther, R. and Krag, H., "The Inter-Agency Space Debris Coordination Committee – An overview of the IADC annual activities Overview of IADC," *2nd ICAO/UNOOSA Symposium*, Harwell Oxford, UK, 2016, pp. 1–13.
6. Liou, J. C., "An Active Debris Removal Parametric Study for LEO Environment Remediation," *Advances in Space Research*, Vol. 47, No. 11, 2011, pp. 1865–1876.
7. Liou, J.-C. and Johnson, N. L., "Risks in Space from Orbiting Debris," *Science*, Vol. 311, No. 5759, jan 2006, pp. 340–341.
8. Biesbroek, R., "The e.Deorbit CDF Study," Tech. rep., Montréal, Canada, 2012.
9. Botta, E. M., Sharf, I., Misra, A. K., and Teichmann, M., "On the Simulation of Tether-Nets for Space Debris Capture with Vortex Dynamics," *Acta Astronautica*, Vol. 123, 2016, pp. 91–102.
10. Botta, E. M., Sharf, I., and Misra, A. K., "Contact Dynamics Modeling and Simulation of Tether Nets for Space-Debris Capture," *Journal of Guidance, Control, and Dynamics*, Vol. 40, No. 1, 2017, pp. 110–123.
11. Benvenuto, R. and Lavagna, M., "Flexible Capture Devices for Medium To Large Debris Active Removal: Simulations Results To Drive Experiments," *12th Symposium on Advanced Space Technologies in Automation and Robotics*, Noordwijk, The Netherlands, 2013.
12. Benvenuto, R. and Lavagna, M., "Net Capturing of Tumbling Space Debris: Contact Modelling Effects on the Evolution of the Disposal Dynamics," *13th Symposium on Advanced Space Technologies in Automation and Robotics*, Noordwijk, The Netherlands, 2015.
13. Benvenuto, R., Lavagna, M. R., and Salvi, S., "Multibody Dynamics Driving GNC and System Design in Tethered Nets for Active Debris Removal," *Advances in Space Research*, Vol. 58, No. 1, 2016, pp. 45–63.
14. Shan, M., Guo, J., and Gill, E., "Deployment Dynamics of Tethered-net for Space Debris Removal," *Acta Astronautica*, Vol. 132, 2017, pp. 293–302.
15. Medina, A., Cercòs, L., Stefanescu, R., Benvenuto, R., Lavagna, M., Gonzalez, I., Rodriguez, N., and Ormnes, K., "Capturing Nets for Active Debris Removal: A Follow-Up on Microgravity Experiment Design To Validate Flexible Dynamic Models," *13th Symposium on Advanced Space Technologies in Automation and Robotics*, Noordwijk, The Netherlands, 2015.
16. Cercos, L., Stefanescu, R., Medina, A., Benvenuto, R., Lavagna, M., Gonzalez, I., Rodriguez, N., and Wormnes, K., "Validation of a Net Active Debris Removal Simulator Within Parabolic Flight Experiment," *International Symposium on Artificial Intelligence, Robotics and Automation in Space*, Montreal, Quebec, Canada, 2014.
17. Lavagna, M. R., Armellin, R., Bombelli, A., Benvenuto, R., and Carta, R., "Debris Removal Mechanism Based on Tethered Nets," *International Symposium on Artificial Intelligence, Robotics and Automation in Space*, Turin, Italy, 2012.
18. Forshaw, J. L., Aglietti, G. S., Navarathinam, N., Kadhem, H., Salmon, T., Pisseloup, A., Joffre, E., Chabot, T., Retat, I., Axthelm, R., Barraclough, S., Ratcliffe, A., Bernal, C., Chaumette, F., Pollini, A., and Steyn, W. H., "RemoveDEBRIS: An In-orbit Active Debris Removal Demonstration Mission," *Acta Astronautica*, Vol. 127, 2016, pp. 448–463.
19. Shan, M., Guo, J., Gill, E., and Gołębiowski, W., "Validation of Space Net Deployment Modeling Methods Using Parabolic Flight Experiment," *Journal of Guidance, Control, and Dynamics*, Vol. 40, No. 12, 2017, pp. 3319–3327.
20. Benvenuto, R., Salvi, S., and Lavagna, M., "Dynamics analysis and GNC design of flexible systems for space debris active removal," *Acta Astronautica*, Vol. 110, 2015, pp. 247–265.
21. Shan, M., Guo, J., and Gill, E., "Contact Dynamics on Net Capturing of Tumbling Space Debris," *Journal of Guidance, Control, and Dynamics*, 2018.
22. Liu, L., Shan, J., Ren, Y., and Zhou, Z., "Deployment dynamics of throw-net for active debris removal," *65th International Astronautical Congress*, 2014.
23. Mankala, K. K. and Agrawal, S. K., "Dynamic Modeling and Simulation of Satellite Tethered Systems," Vol. 127, No. April, 2005, pp. 144–156.
24. Shuai, G., Yong, Y., Xiaofeng, S., and Yuhao, S., *Dynamic Simulation of Fishing Net Based on Cubic B-Spline Surface.*, 2012.
25. Stadnyk, K. and Ulrich, S., "Validating the Deployment of a Novel Tether Design for Orbital Debris Removal," *Journal of Spacecraft and Rockets*, Vol. 57, No. 6, 2020, pp. 1335–1349.
26. Hovell, K. and Ulrich, S., "Postcapture Dynamics and Experimental Validation of Subtethered Space Debris," *Journal of Guidance, Control, and Dynamics*, Vol. 41, No. 2, 2018, pp. 519–525.
27. Hovell, K. and Ulrich, S., "Attitude Stabilization of an Unknown and Spinning Target Spacecraft Using a Visco-Elastic Tether," *13th Symposium on Advanced Space Technologies in Robotics and Automation*, Noordwijk, The Netherlands, 2015.
28. Hovell, K. and Ulrich, S., "Attitude Stabilization of an Uncooperative Spacecraft in an Orbital Environment using Visco-Elastic Tethers," *AIAA Guidance, Navigation, and Control Conference*, San Diego, CA, 2016.

29. Hovell, K. and Ulrich, S., "Experimental Validation for Tethered Capture of Spinning Space Debris," *AIAA Guidance, Navigation, and Control Conference*, Grapevine, TX, 2017.

30. McKnight, D., Witner, R., Letizia, F., Lemmens, S., Anselmo, L., Pardini, C., Rossi, A., Kunstadter, C., Kawamoto, S., Aslanov, V., Dolado Perez, J. C., Ruch, V., Lewis, H., Nicolls, M., Jing, L., Dan, S., Dongfang, W., Baranov, A., and Grishko, D., "Identifying the 50 Statistically-most-concerning Derelict Objects in LEO," *Acta Astronautica*, Vol. 181, No. November 2020, 2021, pp. 282–291.

31. CONFERS, "CONFERS On-Orbit Servicing Mission Phases," Tech. rep., 2019.

32. Hughes, P. C., *Spacecraft Attitude Dynamics*, Dover Publications, Mineola, NY, 2004.

33. Picone, J. M., Hedin, A. E., Drob, D. P., and Aikin, A. C., "NRLMSISE-00 Empirical Model of the A: Statistical Comparisons and Scientific Issues," *Journal of Geophysical Research: Space Physics*, Vol. 107, No. A12, 2002, pp. 1–16.